Journal of Applied Fluid Mechanics, Vol. 18, No. 4, pp. 1023-1034, 2025.
Available online at www.jafmonline.net, ISSN 1735-3572, EISSN 1735-3645.
https://doi.org/10.47176/jafm.18.4.2927

Characteristics of an Internal Dielectric Barrier Discharge Plasma-induced Blowing Device

Y. Zhang[1, 2], B. Dong[1, †], D. Yang[1], X. Yan[2] and Y. Li[2]

[1] *High Speed Aerodynamics Institute, China Aerodynamics Research and Development Center, Mianyang, 621000, China*
[2] *College of Mechanical and Electrical Engineering, Wenzhou University, Wenzhou, 325035, China*

†*Corresponding Author Email: dongbin@cardc.cn*

ABSTRACT

This paper investigates the blowing characteristics of internal dielectric barrier discharge (IDBD) plasma actuators and their application in the flow control field. The effects of different internal channel parameters and the number of actuators on the performance of the IDBD plasma exciter are evaluated using PIV experiments. The results show that the internal actuators are effective in generating blowing with a certain kinetic energy at the outlet, with a velocity of up to 1.5 m/s. The blowing characteristics are significantly affected by the channel height (H) and outlet length (L). Deflection of the channel inlet or outlet introduces more possibilities for the installation of IDBD plasma actuators, albeit with a loss of about 15% of the kinetic energy of the blowing. With a modulated wave setup, the plasma actuator allows for unsteady blowing and generates frequency-controllable vortices, providing new possibilities for active control of frequency-specific wake streams. In addition, the flow control performance of the IDBD plasma actuator is demonstrated in the wake of a plate with a blunt trailing edge (TE), confirming the actuator's ability to alter the flow pattern and reduce the characteristic frequency. Despite the limitations of actuators in energy efficiency, the IDBD plasma actuator still shows great potential for flow control while increasing resistance to environmental effects.

Article History

Received June 20, 2024
Revised September 8, 2024
Accepted October 20, 2024
Available online February 4, 2025

Keywords:

IDBD plasma actuator
Flow control
Blowing characteristic
Steady blowing
Unsteady blowing

1. INTRODUCTION

Flow control through plasma actuators is an emerging technology based on plasma aerodynamic excitation, offering advantages such as a simple structure and fast response. Among these technologies, the dielectric barrier discharge (DBD) plasma actuator stands out for its stable operating conditions, making it widely used in the field of flow control (Moreau, 2007; Wang et al., 2013). As shown in Fig. 1, the DBD plasma actuator consists of an upper (exposed) electrode and a lower (embedded) electrode, with the lower electrode covered by a dielectric material. The asymmetrical arrangement of the electrodes generates an induced flow, commonly referred to as ionic wind, which provides the actuator with its control authority. Roth (1995) and Roth et al. (2000) conducted the first study on atmospheric uniform glow discharge plasma in 1995. Since then, researchers have explored various applications of DBD plasma actuators, including the control of blunt body wake (Jukes & Choi, 2009; Kozlov & Thomas, 2011; Kazanskyi et al., 2012; Lee et al., 2022), suppression of hydrodynamic noise

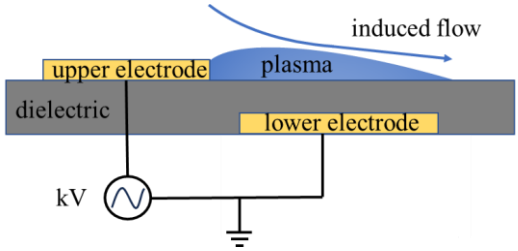

Fig. 1 Schematic of a DBD actuator

(Huang & Zhang, 2008; Li et al., 2010; Kopiev et al., 2014; Zhang et al., 2022), tripping of the boundary layer (Rizzetta & Visbal, 2010; Visbal, 2010; Yu et al., 2014; Ogawa et al., 2022), and unsteady characterization processes in the shear layer (Grundmann & Tropea, 2007; Chernyshev et al., 2011; Ely & Little, 2013; Yu et al., 2023). The excellent control capabilities and low-cost efficiency of these actuators have secured their place in active flow control.

Researchers have conducted both numerical and experimental studies on DBD plasma actuators. Numerical modeling of DBD actuators provides a

NOMENCLATURE

C	chord length of flat plate	S	single-side plasma actuator
D	double-side plasma actuator	T	period of actuator startup
f_1	frequency of square AC wave	t	the thickness of the actuator models
f_2	frequency of modulated wave	U, V	the blowing flow velocity (streamwise and vertical,)
f_{vs}	frequency of vortex shedding	U_{max}	maximum flow velocity
H	height of the channel	U_∞	velocity of freestream
h	thickness of flat plate	V_{pp}	amplitude of square AC wave
L	length of the outlet	x, y, z	Cartesian coordinates (streamwise, vertical, and spanwise directions)
Q	mean blowing flow rate	λ	wavelength of vortex shedding
Re_c	Reynolds number based on the chord length	ΔL_p	reduction in peak sound pressure level

valuable tool for evaluating their performance. One of the most widely used models in engineering applications is the Suzen-Huang model. Bernal-Orozco et al. (2023) evaluated the performance of this model under various operational and geometrical parameters. While the model successfully reproduced the structure of the induced flow, it underestimated the electrohydrodynamic forces and induced flow velocity of the actuator. Nesaeian and Homaeinezhad (2023) numerically proposed a surface DBD analytical model (SDBD-AM) based on the flat plate DBD model. They attributed the observed effects to structural factors such as electrode width, electrode spacing, dielectric properties, and environmental influences, noting that the uncertainties varied depending on each factor. Moayedi et al. (2023) numerically simulated actuator performance using the finite volume method (FVM), incorporating the plasma body force into the momentum term as a source term. Their study primarily investigated the effects of Reynolds number, applied voltage, and voltage frequency on the performance of the DBD plasma actuator. Similarly, Seth et al. (2018) performed numerical simulations to analyze the impact of electrical and geometrical parameters on the operating characteristics of DBD plasma actuators. They evaluated factors such as dielectric thickness, electrode gap, applied voltage frequency, and waveform, showing that maximum ionic velocity increases with higher applied voltage and a reduced gap between electrodes. Erfani et al. (2013) investigated the design of multiple encapsulated electrodes for DBD plasma actuators to achieve higher induced ionic velocity. They performed numerical optimization to determine the best actuator configuration and validated their findings experimentally. Wang et al. (2022) also carried out numerical simulations using a body force model to explore the effects of duty cycle and unsteady excitation on flow structures using Lagrangian coherent structures.

In the experimental field, many studies have thoroughly examined the electrical and geometrical parameters of DBD plasma actuators, particularly focusing on plasma-induced flow velocity and momentum properties (Sun et al., 2023). Erfani et al. (2015) explored the variation in induced flow velocity for different DBD plasma actuators with varying numbers and distributions of encapsulated electrodes within the dielectric layer. Wojewodka et al. (2020) experimentally characterized the performance of surface and channel plasma actuators using a Pitot tube and PIV device. Their results on velocity distribution revealed a high gradient of velocity reduction with streamwise distance, indicating that plasma actuators primarily have localized effects. Thomas et al. (2009) further verified the consistency between reaction forces and flow momentum by integrating the velocity distribution downstream of the actuator. Conversely, Enloe et al. (2004) demonstrated that the maximum velocity induced by a plasma actuator is limited by the area covering the electrodes as the AC amplitude increases. This limitation is due to the dielectric area being insufficient to store the charge necessary to fully utilize the applied voltage, a phenomenon known as the self-limiting factor of AC DBD plasma actuators. Studies have recorded maximum induced velocities of up to 10 m/s (Huang & Zhang, 2008; Cattafesta & Sheplak, 2011). In experiments conducted by Hehner et al. (2023), the spatio-temporal body force distributions in both quiescent and external airflow environments were compared to analyze the ability of the actuator-generated momentum to be transferred to the surrounding fluid. It was found that the shape of the spatio-temporal body force distribution changes as the airflow velocity increases, while the magnitude of the integral force remains approximately constant.

In terms of applications, plasma actuators are often used to improve the aerodynamic performance of equipment. Lombardi et al. (2013) utilized a plasma actuator for the closed-loop control of dynamic stall on an airfoil. When the pressure fluctuation at the leading edge exceeded a predetermined value, the actuator initiated high-power excitation control. This closed-loop control increased the combined lift over the entire cycle by 12% and reduced the maximum pitching moment by 60%. Similarly, plasma actuators have been shown to increase lift for flow field control around a cylinder and enhance flow circulation (Uemura et al., 2023). Luo and Li (2022) investigated the characteristics of SD actuators, finding that plasma excitation altered the mean velocity and turbulence intensity of the cylindrical wake, which inhibited flow separation or increased flow losses. Guo et al. (2023) explored the coherent structure of the flow field generated by sliding dielectric barrier discharge and its spatial effect, finding that the DBD induces vortex structures in the downstream region of the electrodes and enhances the mixing and squeezing effects of the upper and lower flow fields. Al-Sadawi and Chong (2016) examined the effects of different DBD plasma actuator configurations on vortex shedding noise and wake flow,

discovering that "downward" plasma actuation can nearly eliminate vortex shedding noise at the pitch frequency by effectively increasing the vortex shedding frequency. Yan et al. (2024) effectively altered the vortex shedding pattern at the trailing edge (TE) of a plate and reduced the associated tonal noise using a DBD plasma actuator.

In summary, although plasma actuators demonstrate excellent active control in terms of aerodynamics, they have significant limitations regarding amplitude and energy efficiency. Additionally, the exposure of electrodes in the external plasma can limit their resistance to interference during application. To address this issue and improve the actuator's ability to resist environmental influences, this paper departs from most previous studies by placing the plasma device in a slit, thereby proposing the concept of an internal dielectric barrier discharge (IDBD) plasma actuator. A simple experimental model is used to validate this concept. The internal slits effectively utilize the aerodynamic active control function of the actuator while substantially increasing its resistance to interference. The deflection of the slits in the IDBD actuator offers additional possibilities for flow control with minimal loss of kinetic energy. The paper is structured into four sections: Section II describes the experimental setup, including the actuator configuration and measurement methods; Section III presents and discusses the experimental results of flow measurements; and Section IV provides the main conclusions of the study.

2. EXPERIMENTAL SETUP

2.1 IDBD Plasma Actuator Setup

Figure 2 shows the schematic diagram of a plasma actuator. It consists of two electrodes and a dielectric layer, where both electrodes are made of copper foil with a thickness of 0.05 mm, and the width of the exposed electrode is 5 mm, while that of the encapsulated electrode is 10 mm. Selecting a thin dielectric material improves the performance of the actuator (Wojewodka, et al., 2020). The dielectric layer consists of an insulating plexiglass sheet. The actual operating condition of the actuator is shown in Fig. 2(b). The induced airflow generated by the plasma begins to move downstream from the exposed electrode. Figure 2(c) displays the power switching circuit topology of the power system. A DC supply provides a voltage of 45 V, which, after being stepped up by an ignition coil with a transformer ratio of 1:500, yields an output of approximately 22.5 kV AC from the step-up transformer. A function generator is used to generate a square AC wave with an amplitude of V_{pp}=10 V and a frequency of f_1 = 6 kHz. The duty cycle is 50%. In a study by Wojewodka et al. (2020), it was demonstrated that both excessively high and low frequencies increase the power consumption of the actuator. The drive signal activates an Insulated Gate Bipolar Transistor (IGBT) module, which then applies the high AC voltage to the exposed electrodes to induce discharge, while the encapsulated electrodes remain grounded. Throughout this process, the high-voltage AC ionizes the air near the exposed electrodes, creating an atmospheric glow discharge plasma that exerts a plasma force on the surrounding air. This force accelerates the airflow along the surface of the actuator.

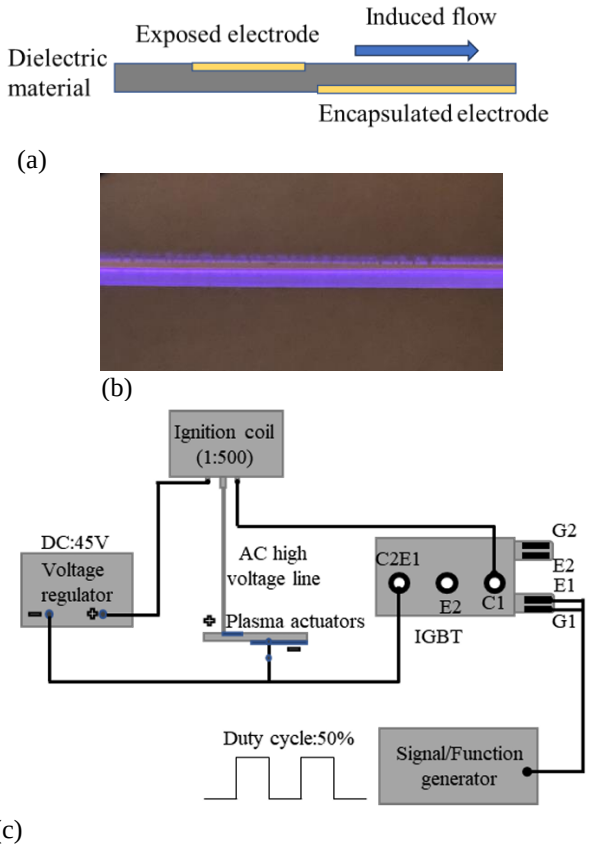

Fig. 2 Plasma actuator setup (not to scale): (a) electrode setup; (b) excited state; (c) power supply circuit

Additional details regarding the actuator can be found in previous research (Yan et al., 2024).

Figure 3 shows a two-dimensional (2-D) schematic of the installation of the internal actuator. The actuators are all embedded in different internal channel models to increase their resistance to environmental influences. There are three types of internal channels for plasma-induced airflow: Model 1 (M1) for horizontal blowing and suction, Model 2 (M2) for horizontal suction and vertical blowing, and Model 3 (M3) for vertical blowing and suction. All channels are made of resin material via 3D printing. The actuators are arranged on both the upper and lower surfaces within the channel. The thickness t is 10 mm for all models. For consistency in channel length, the thicknesses of the deflected outlet and inlet are also t for both M2 and M3. The performance of a single-side (S-) and a double-side (D-) plasma actuators was tested separately during the experiment. All actuators are positioned 20mm from the inlet of the channel and L from the outlet, with four groups of outlet lengths are designed with L=20 mm, 40 mm, 60 mm, and 80 mm (L20, L40, L60, L80). The corresponding dimensionless parameters are L/t = 2, 4, 6, 8. The height of the channel is H, with two sets of heights with H=2 mm and 4mm (H2, H4) were used. The detailed parameters of all models are shown in Table 1. For convenience, numbers are used for representation throughout the following sections. In addition, the Cartesian coordinate origin of all models is located at the outlet.

Table 1 Parameters of the model configuration

actuator	outlet (*L*, mm)	channel (*H*, mm)
single (S-)	20, 40, 60, 80	2, 4
double (D-)		

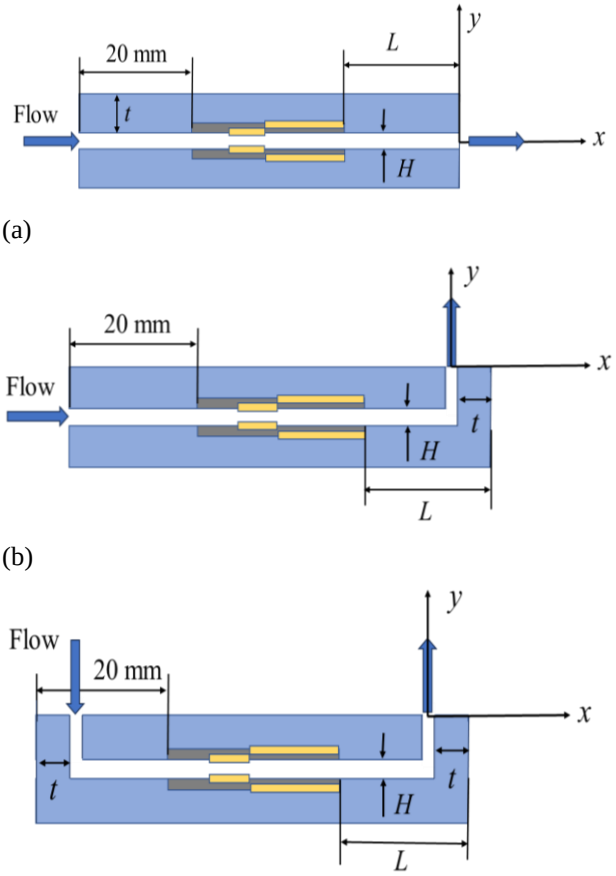

Fig. 3 Internal plasma actuator setup; (a) M1; (b)M2; (c)M3

2.2 Particle Image Velocimetry (PIV) Measurements

To visualize the blowing structure generated by the plasma as it passing through the channel, PIV measurements were performed on all models. The experiments were conducted within an anechoic chamber at Wenzhou University (WZU), measuring 3.8 meters in length, 3.5 meters in width, and 2.5 meters in height. This chamber has a cutoff frequency of 140 Hz and is lined with acoustic wedges that stand 0.6 meters tall to ensure optimal sound isolation. The specifics of the wind tunnel used in these experiments have been documented by Niu et al. (2022). Figure 4 shows a 2-D schematic of the PIV measurements. The test areas are all in the middle plane (z=0) of the model's spreading direction to observe representative flow structures. The model was placed in a particle box made of transparent plexiglass. Tracer particles were filled in the box before the start of the experiment to ensure visualization of the flow structure. The support platform raised the model to a certain height, thereby eliminating the effect of the ground on the plasma-induced blowing.

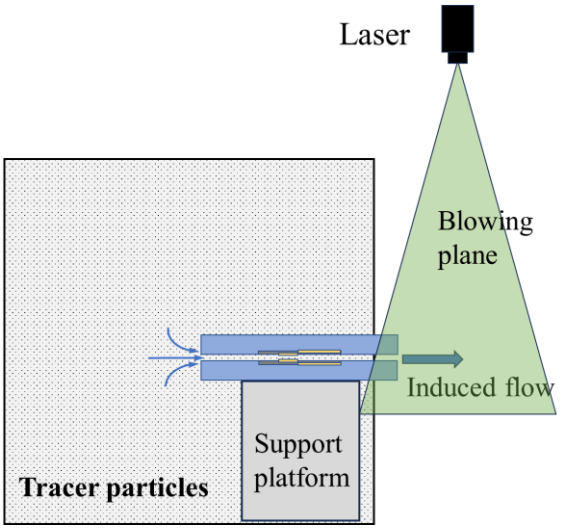

Fig. 4 PIV measurement setup

The experimental apparatus was equipped with a double-pulse New Wave Gemini Neodymium-Doped Yttrium Aluminum Garnet (Nd:YAG) laser, which reached a maximum output of 120 mJ. The laser was set to produce a laser sheet with a consistent thickness of approximately 1 mm within the region of interest of the model. To capture high-resolution images, a Nikon charge-coupled device (CCD) camera with a resolution of 2456×2672 pixels was used. Tracer particles, with an average diameter of approximately 1 μm, were introduced into the flow by burning sulfur powder, helping to delineate the flow patterns. The experimental procedure involved acquiring a dataset of 400 images for each experimental condition. After image capture, each set was processed using cross-correlation analysis over a 64×64 pixels interrogation area, with a 50 percent overlap to enhance data reliability. The authors estimated that the uncertainty of the velocity field and vorticity to be within 2% (Raffel et al., 2018).

3. RESULTS AND DISCUSSION

3.1 Steady Blowing

Due to the geometrical limitations of the channel model, the PIV measurements could not display the flow field inside the channel, but visualization was conducted downstream of the outlet. Figure 5 shows the average velocity field (including velocity vector distribution) and its corresponding smoke map for model M1 with a single side of the plasma actuator turned on. The model outlet demonstrates significant blowing characteristics at a channel height of 2 mm, and the average velocity distribution aligns with the results obtained by Wojewodka et al. (2020). As shown in Fig. 5(a), the plasma actuator produces blowing at the outlet by transferring kinetic energy to the air, with the central velocity reaching about 1.0 m/s. When the channel height is increased to 4 mm, the width of the blowing justifiably becomes larger, and the kinetic energy of the airflow increases, as indicated by the rise in the center velocity to approximately 1.5 m/s, as shown in Fig. 5(c).

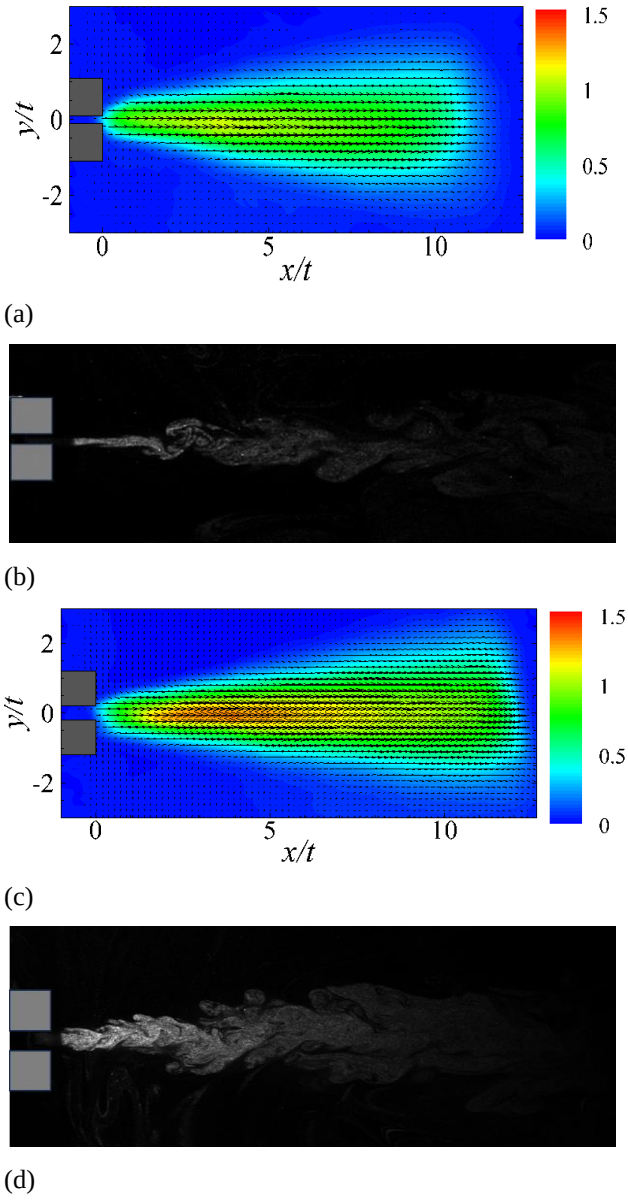

Fig. 5 Contour of average velocity for M1 under the single-side plasma actuator and its smoke map: (a) and (b) for S-*H*2 *L*20; (c) and (d) for S-*H*4 *L*20

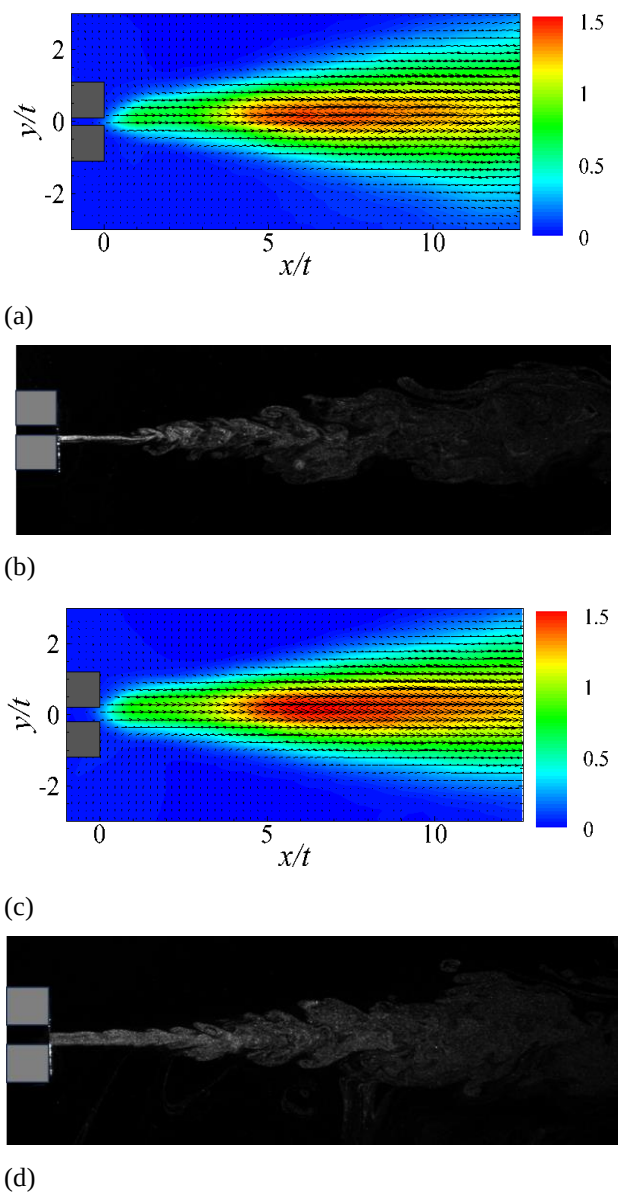

Fig. 6 Contour of average velocity for M1 under the double-side plasma actuators and its smoke map: (a) and (b) for D-*H*2 *L*20; (c) and (d) for D-*H*4 *L*20

Figure 6 illustrates the contour of average velocity and smoke map of M1 with the double-side plasma actuators turned on. The kinetic energy of the blowing generated by the double-side actuators is significantly increased compared to the single-side. The core region of the blowing at the outlet is increased considerably and the position is shifted backward. It is clearly observed in the smoke maps that the stabilization length of the shear layer at the outlet increases due to the increase in kinetic energy of the blowing, and the destabilization of the shear layer occurs at a more downstream location. In addition, a cluster of tracer particles ejected from the channel can still be observed farther downstream. As shown in Fig. 6(a) and (c), the core of the blowing remains prominent at x/t=10 in the velocity contour. This indicates that double-side plasma actuators have a greater potential for active control. Similarly, the larger channel height, represented by H=4 mm, produces a higher kinetic energy blowing, which suggests that when applying plasma actuator channels, increasing the height of the internal channel can allow for more airflow to enter.

To further compare the effect of outlet length on the blowing produced by the actuator channel, the blowings with L/t=4, 6, and 8 (L=40 mm, 60 mm, 80 mm) were also measured, as shown in Fig. 7. At L/t=4, the kinetic energy of the blowing generated by H=4 mm remains significantly higher than that generated by H=2 mm, even though the outlet length is doubled. As the outlet length increases, the area affected by the blowing decreases, with more flow features produced by the plasma located outside the PIV view, i.e., inside the channel. However, the flow velocity in the core region of the blowing remains around 1 m/s.

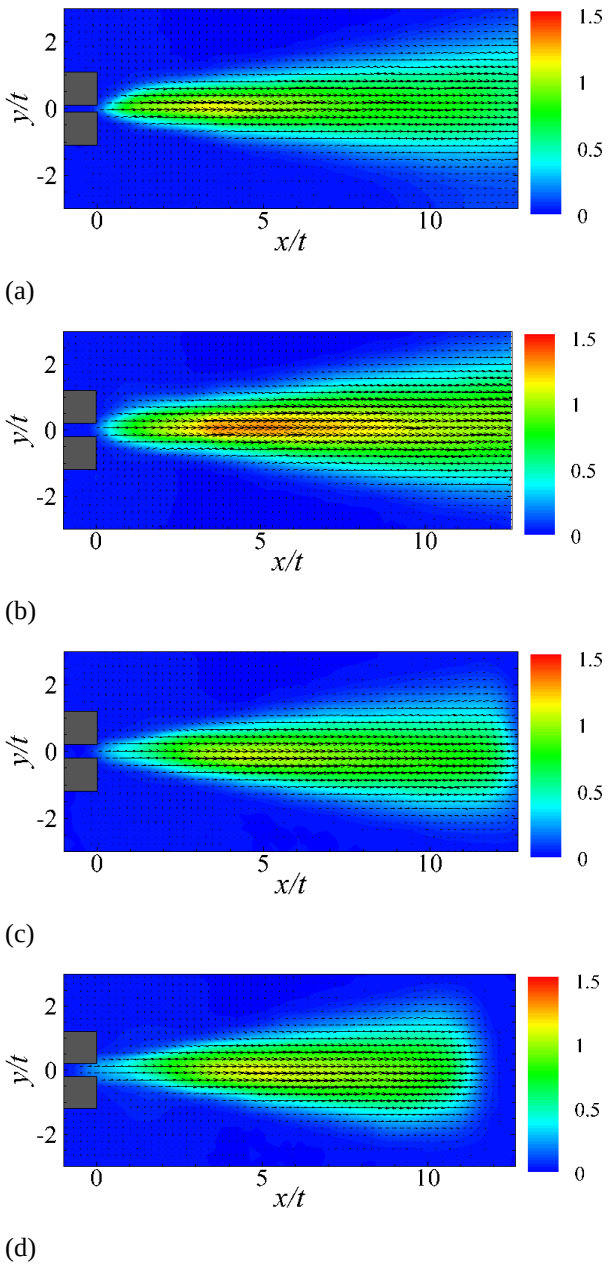

Fig. 7 Contour of average velocity of M1 under the double-side plasma actuators: (a) D-*H*2 *L*40; (b) D-*H*4 *L*40; (c) D-*H*4 *L*60; (d) D-*H*4 *L*80

To quantitatively analyze the blowing characteristics generated by the IDBD actuators, the average flow velocity profiles for model M1 at *x*/*t*=5, 8, and 12 are provided in Fig. 8. From the velocity profiles in the first row, it is evident that the kinetic energy of the blowing generated by the double-side actuators is higher than that of the single-side actuators across all measured profiles. Farther downstream, at *x*/*t*=12, the velocity of the blowing produced by the single-side actuator gradually approaches zero. A high velocity reduction gradient is observed along the flow distance, reflecting the fact that plasma actuators typically have localized effects (Wojewodka et al., 2020). However, the blowing velocity of the double-side actuators remains above 1 m/s at this point, and the kinetic energy dissipation is slower. The velocity drop gradient over the flow distance is reduced significantly, overcoming the localized effects to some extent. The second row of velocity profiles compares the variation across different outlet lengths. As the outlet length increases, the airflow generated by the actuator has to pass through a longer internal channel before forming induced blowing downstream. Wall friction losses rise significantly with increasing length, leading to a marked reduction in blowing velocity at the outlet, especially at *L*/*t*=8. Therefore, for optimal flow control, the placement of the actuator is particularly important.

On the *x*/*t*=5 profile, the blowing characteristics are fully exhibited in the range of *y*/*t*=-2 to 2. Therefore, the velocity distribution within this region is integrated to obtain the mean blowing flow rate, which is used as a measure of blowing intensity (Thomas et al., 2009). Here, y_1 is 20 mm. The mean blowing flow rate is defined as:

$$Q = \int_{-y_1}^{y_1} U(y)dy \tag{1}$$

Table 2 shows the magnitude of the average flow rate produced for different model configurations. With the configuration of D-*H*4 *L*20, the average flow rate in the blowing region reaches a maximum of 3.114×10^{-2} m^2/s. When the outlet length is increased to 60 mm or 80 mm, the outlet flow rate decreases to about half of the maximum. At the same height and length as the maximum flow rate (*H*4 *L*20), the outlet flow rate generated by the single-sided plasma actuator remains 2.132×10^{-2} m^2/s, suggesting that the benefit of the double-sided actuators to the IDBD plasma blowing is not multiplicative, which may be related to the air volume limitation inside the channel.

The kinetic energy of the blowing generated at the outlet was used as a measure of the plasma actuator's energy. Based on the flow rates in Table 2, the energy distribution of the actuator is shown in Fig. 9. The maximum flow velocity U_{max} at the same location is also plotted in Fig. 9. The variation patterns of U_{max} and flow rate are essentially the same across these seven models. An increase in outlet length inevitably causes a reduction in kinetic energy, thus reducing the energy generated by the actuator at the outlet. Increasing the number of actuators (i.e., using double-sided actuators) significantly increases the blowing velocity and flow rate at the outlet, but not exponentially. The height of the channel only provides a small increase in the energy efficiency of the actuators. Therefore, when using IDBD actuators for flow control, the effects of outlet length, number of actuators, and channel height must be considered simultaneously.

Table 2 Actuator energy in different states

Model	Location	Range of points, mm	Flow rate ($\times10^{-3}$), m^2/s
S-*H*2 *L*20	*x*/*t*=5	（-20, 20）	17.62
S-*H*4 *L*20			21.32
D-*H*2 *L*20			29.63
D-*H*4 *L*20			31.14
D-*H*4 *L*40			18.72
D-*H*4 *L*60			14.93
D-*H*4 *L*80			16.03

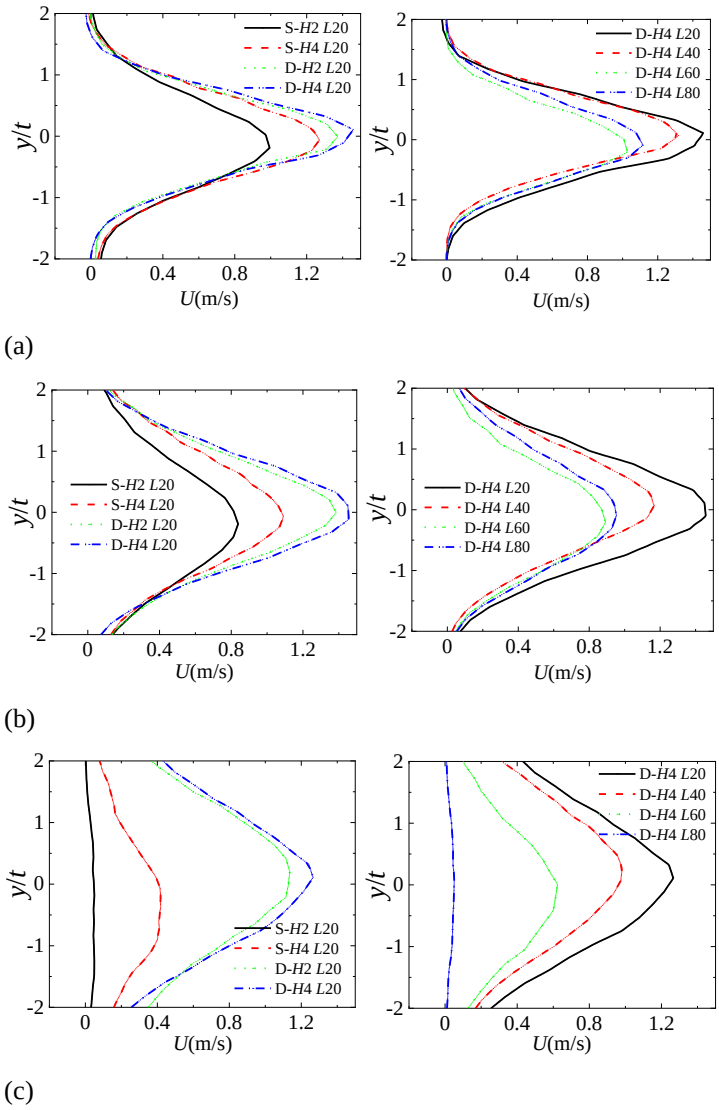

Fig. 8 Average velocity profiles of model M1 at different locations: (a) *x/t*=5; (b) *x/t*=8; (c) *x/t*=12

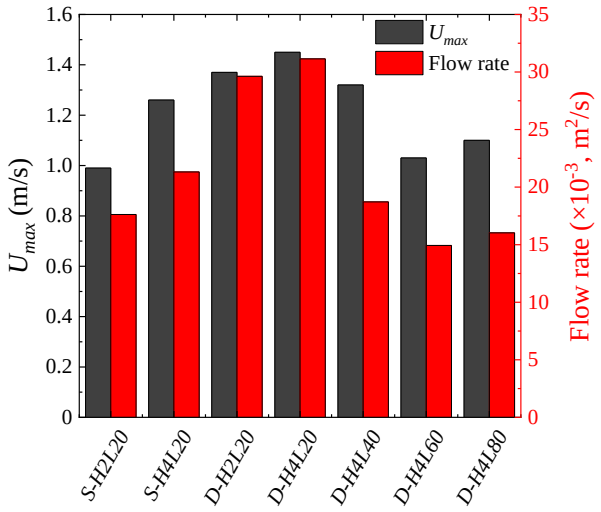

Fig. 9 Energy comparison of different models

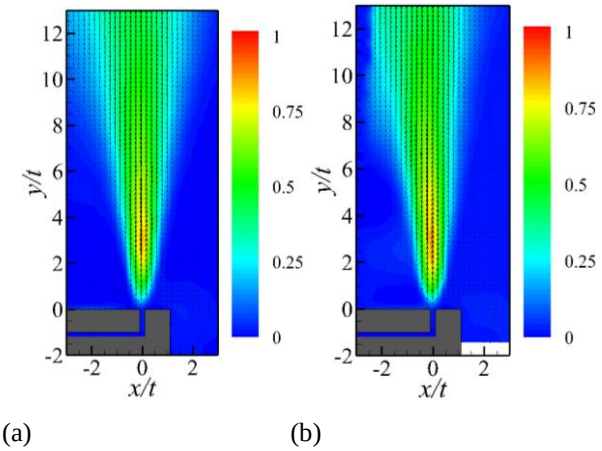

Fig. 10 Contour of average velocity under S-*H2 L20* actuator: (a) M2; (b) M3

Figures 10(a) and (b) show the average blowing velocity contour for the deflected channels, i.e., models M2 and M3. Figure 11 provides the velocity profiles at 3*t* and 8*t* downstream of the outlet. Whether only the outlet is deflected (M2) or both the inlet and outlet channels are deflected (M3), the variation of the blowing characteristics at the outlet shows a similar behavior. Due to the vertical deflection of the airflow in the channel, both M2 and M3

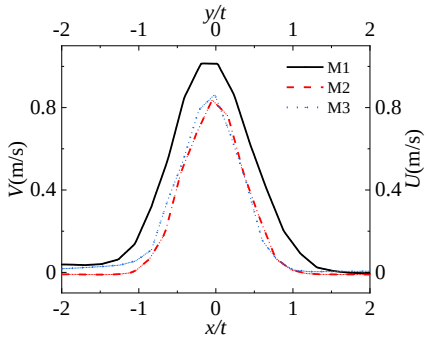

(a)

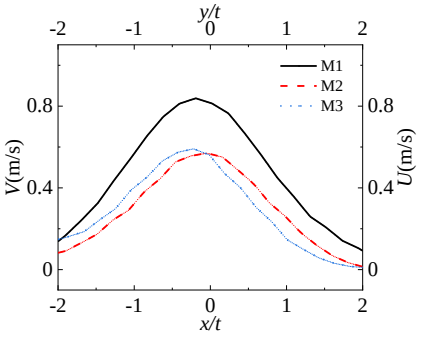

(b)

Fig. 11 Profile of average velocity under S-*H*2 *L*20 actuator: (a) 3*t* downstream of the outlet; (b) 8*t* downstream of the outlet

exhibit a velocity deficit compared to the M1 model. Using the velocity profile at 3*t* downstream of the outlet as a reference, the rate of kinetic energy loss of the blowing is about 15% for both M2 and M3. Therefore, the kinetic energy loss of the induced blowing is a non-negligible issue when using IDBD plasma actuators with internal corners.

3.2 Unsteady Blowing

The flow condition of the IDBD plasma actuators under steady conditions was discussed in Section 3.1. For the unsteady conditions, a signal generator produced a high-frequency excitation at 6 kHz. In this case, the temporal scale of the alternating current (AC) signal driving plasma formation is considerably brief compared to the relevant temporal scales of the flow dynamics. Consequently, the body force generated by the plasma can be regarded as quasi-steady within the context of the flow being investigated. In the original setup of the steady plasma actuator, an additional modulated wave signal was applied to the actuator by a signal function generator, as shown in Fig. 12. Due to experimental equipment

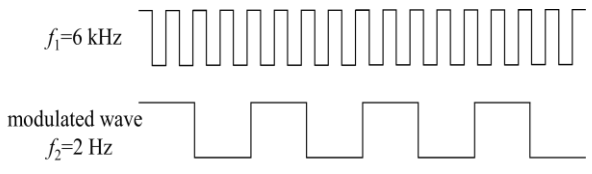

Fig. 12 Unsteady actuation signal (not to scale)

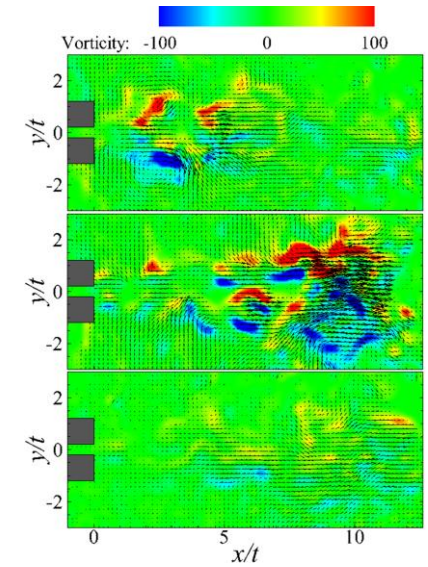

(a)

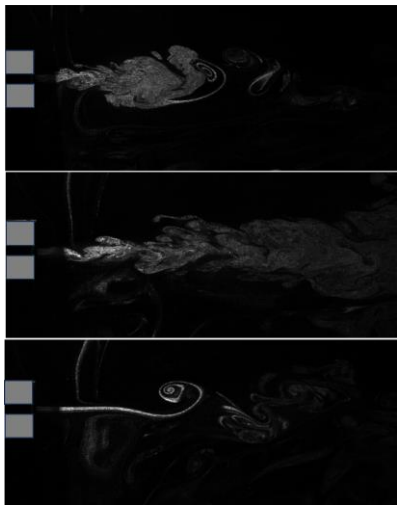

(b)

Fig. 13 Contour of instantaneous vorticity of M1 in the S-*H*4 *L*20 for one period *T* under the modulated wave and its smoke map: (a) instantaneous vorticity contour (b) smoke map

limitations, only the frequency f_2=2Hz was selected for measurement in this paper. The signal sent to the actuator under the action of the modulated wave had the characteristic frequency f=f_2.

Figure 13 shows the instantaneous vorticity contour and smoke maps of model M1 for one period T in the state with the single-side actuator turned on. The plasma-induced flow was periodically ejected from the outlet, forming induced vortex clusters that shed and propagated downstream at a non-stationary plasma drive frequency. This indicates that the non-stationary blowing is capable of inducing vortices with controllable frequencies. To control a fixed-frequency wake, such as the classical Kármán vortex street, the vortices induced by non-stationary blowing can cancel out coherent vorticity of opposite sign (Thomas et al., 2008).

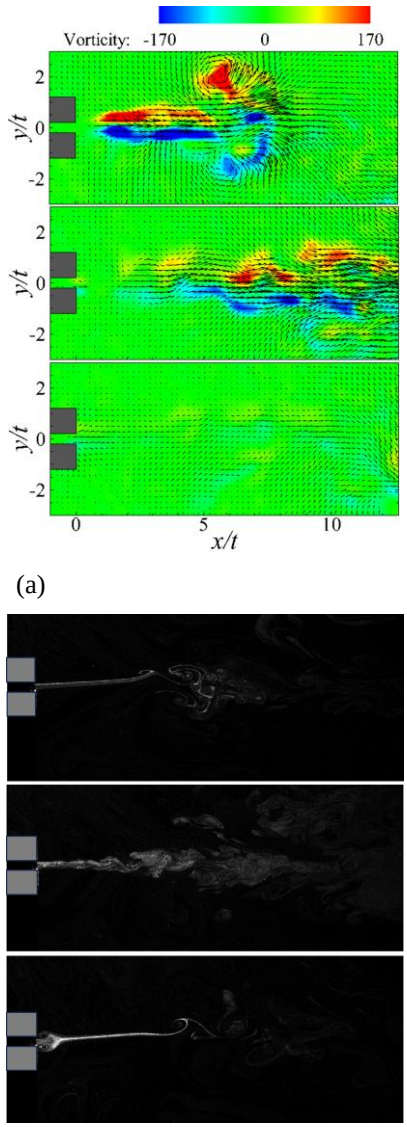

Fig. 14 Contour of instantaneous vorticity of M1 in the D-*H*4 *L*20 for one period *T* under the modulated wave and its smoke map: (a) instantaneous vorticity contour (b) smoke map

Figure 14 shows the instantaneous vorticity contour and smoke map for one period T with the double-side actuators turned on. The instantaneous vorticity contour located at 1/3T in Fig. 14(a) exhibits a more stable and longer shear layer. This state is suitable for generating stronger vortex impacts and can produce more effective active flow control.

3.3 Active Control of the Plate Wake

In this section, the effect of flow control using IDBD plasma is demonstrated with a blunt trailing edge flat plate. Figure 15(a) shows the 2D cross-section of the plate, which has a chord length of C=200 mm and a thickness of h=10 mm. The Reynolds number (Re_c) based on the chord length is 1.33 × 10^5. An IDBD plasma channel was integrated into a dovetail structure within 40 mm of the trailing edge (TE) to control the wake flow. The plate was placed in the wind tunnel's test section for acoustic and

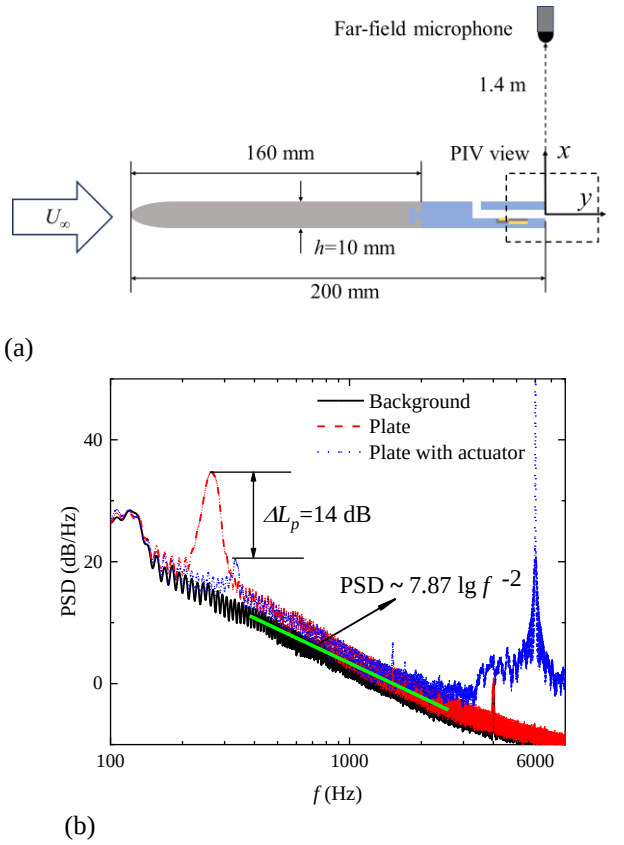

Fig. 15 Plate with blunt TE and its far-field noise spectrum: (a) configuration of plate (b) far-field noise spectrum

flow field measurements at an incoming flow velocity of 10 m/s. A far-field microphone, positioned 1.4 m from the TE of the plate, recorded noise measurements, while PIV measurements focused on the TE. More details are available in Yan et al. (2024).

The far-field noise spectrum is shown in Fig. 15(b). The flat plate exhibited peak noise at specific frequencies, with levels significantly higher than the background noise of the wind tunnel. Across the spectrum, the magnitude of the PSD in logarithmic coordinates is inversely proportional to the square of the frequency, reflecting the typical far-field noise attenuation pattern of a plate. The tonal noise observed at certain frequencies is attributed to vortex shedding behind the blunt TE.

Active control of vortex shedding downstream was achieved by applying a plasma actuator at the TE. The controlled plate produced a distinct narrowband noise at 6 kHz, which corresponded to the actuator's driving frequency f_1. While the actuator's self-noise affected the spectrum above 3 kHz, the most concerning issue was the low-frequency peak noise due to vortex shedding. This vortex shedding not only increases aerodynamic drag but also poses a structural risk if its frequency aligns with the plate's natural frequency, potentially leading to instability or damage (Al-Sadawi et al., 2019). As shown by the blue dotted line in Fig. 15(b), the plasma actuator significantly suppressed the peak noise at the dominant frequency. Compared to the baseline plate, the actuator reduced the peak sound pressure level (ΔL_p) by 14 dB, indicating a

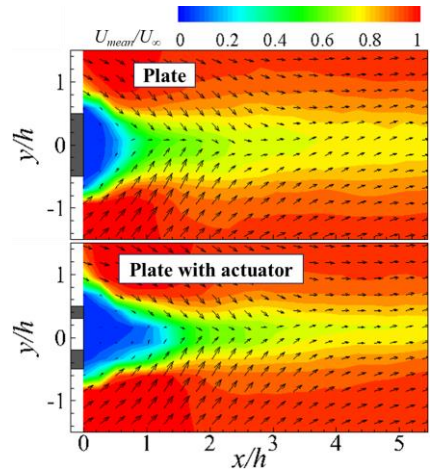

(a)

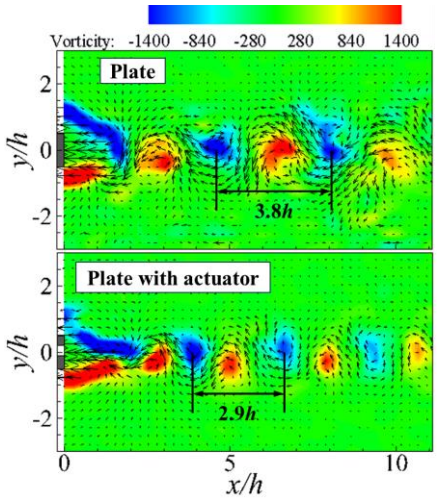

(b)

Fig. 16 Flow field results for a flat plate with and without IDBD plasma excitation: (a) mean velocity (b) instantaneous vorticity

substantial decrease in noise propagation from vortex shedding at the TE. Additionally, the characteristic frequency shifted from 265 Hz to 335 Hz. This upward shift is consistent with findings from Al-Sadawi et al. (2019) and suggests that the IDBD-induced blowing makes the wake's coherent structure more compact, altering the flow pattern at the TE.

Figure 16 shows the results of PIV measurements at the TE. The average streamwise velocity contour in Fig. 16(a) demonstrates that the wake region becomes longer and thinner, with the recirculation zone moving downstream in response to the IDBD plasma actuator. Unlike the surface plasma actuators used by Al-Sadawi & Chong (2016), the IDBD actuator's blowing, originating from within the TE, acted as a virtual separating divider. This reduced interaction between the shear layers and injected energy further downstream. The instantaneous vortex contour in Fig. 16(b) illustrates changes in vortex shedding at the TE. The plasma actuator increased the length of the upper and lower shear layers, and the flow distance λ between consecutive same-side vortices decreased from 3.8h to 2.9h. As a result, the vortex shedding frequency ($f_{vs}=U_\infty/\lambda$) shifted from 263Hz to 344Hz. These changes align with the spectrum shift in Fig. 15(b), confirming that the actuators significantly altered the vortex structure in the wake, and reduced the characteristic frequency of the flat plate.

4. CONCLUSION

This paper presented an experimental study on the characteristics of IDBD plasma-induced blowing devices, highlighting the effectiveness and potential applications of the actuators under different model configurations. The results demonstrate that IDBD plasma actuators are efficient in generating both steady and unsteady blowing at the channel outlet, with performance influenced by the channel height H, outlet length L, and the number of actuators.

For steady blowing, shorter outlet lengths and larger channel heights enable the actuators to produce higher momentum and wider blowing at the outlet. A double-side actuator configuration increases the energy output, but without achieving a multiplicative effect. In the D-H4 L20 configuration, the core blowing velocity reached approximately 1.5 m/s, with the flow rate at 5t downstream of the outlet remaining around 3.114×10^{-2} m^2/s. In addition, deflecting the inlet or outlet broadens the installation options for the IDBD plasma system. Even with a 90° deflection, the blowing energy loss is only about 15%.

The effectiveness of IDBD plasma control was verified through experiments with a blunt TE flat plate. Although the plasma actuator introduced self-noise in the mid- and high-frequency ranges, it significantly reduced peak noise at the vortex shedding frequency, extended the length of the recirculation zone, and achieved active control over the plate wake.

Unsteady blowing was accomplished by modulating the signal, inducing frequency-controlled vortices. Theoretically, these vortices could cancel out coherent vorticity of opposite sign. Although this experiment realized unsteady blowing at only 2 Hz, it offers a new approach to actively controlling wake flow at specific frequencies.

In summary, the IDBD plasma actuator improves environmental resistance by placing the plasma device within a slit. Both steady and unsteady plasma-induced blowing demonstrate significant potential for enhancing aerodynamic performance, offering new strategies for flow separation control, noise suppression, and related applications. However, the experiments were limited to a simple plate model, and the plasma power was constrained, resulting in unsteady blowing at just 2 Hz. Future research should focus on optimizing plasma actuator design to improve energy efficiency and applying modulated waves of multiple frequencies for unsteady blowing and suction at target frequencies. Additionally, addressing the self-noise generated by the plasma, especially at high frequencies, will be critical to expanding its practical use in broader engineering applications.

ACKNOWLEDGEMENTS

This work was made possible through the support provided by the National Natural Science Foundation of China (Grant No. 11972022) and the research grants from Science & Technology Department of Sichuan Province (Grant No. 2023NSFSC0057), which is gratefully acknowledged.

CONFLICT OF INTEREST

The authors have no conflicts to disclose.

AUTHORS CONTRIBUTION

Yaowen Zhang: Formal analysis (equal); Methodology (equal); Writing–original draft (equal); Writing– review & editing (equal). **Bin Dong:** Writing–review & editing (equal). Supervision (equal); Funding acquisition (equal); **Dangguo Yang:** Funding acquisition (equal); Supervision (equal); **Xicai Yan:** Data curation (equal); Formal analysis (equal); **Yong Li:** Conceptualization (equal); Funding acquisition (equal); Methodology (equal).

REFERENCES

Al-Sadawi, L., Chong, T. P., & Kim, J. H. (2019). Aerodynamic noise reduction by plasma actuators for a flat plate with blunt trailing edge. *Journal of Sound and Vibration*, *439*, 173-193. https://doi.org/10.1016/j.jsv.2018.08.029

Al-Sadawi, L. A., & Chong, T. P. (2016). *Vortex shedding noise reduction by single dielectric barrier discharge plasma actuators.* 22nd AIAA/CEAS Aeroacoustics Conference (p. 2759). https://doi.org/10.2514/6.2016-2759

Bernal-Orozco, R. A., Carvajal-Mariscal, I., & Huerta-Chavez, O. M. (2023). Flow and performance effects of a phenomenological model for a DBD actuator under different operating parameters. *Journal of the Brazilian Society of Mechanical Sciences and Engineering*, *45*(10), 513. https://doi.org/10.1007/s40430-023-04436-y

Cattafesta III, L. N., & Sheplak, M. (2011). Actuators for active flow control. *Annual Review of Fluid Mechanics*, *43*, 247-272. https://doi.org/10.1146/annurev-fluid-122109-160634

Chernyshev, S. L., Kiselev, A. P., & Kuryachii, A. P. (2011). Laminar flow control research at TsAGI: Past and present. *Progress in Aerospace Sciences*, *47*(3), 169-185. https://doi.org/10.1016/j.paerosci.2010.11.001

Ely, R., & Little, J. (2013). *Mixing layer excitation by dielectric barrier discharge plasma actuators*. 51st AIAA Aerospace Sciences Meeting including the New Horizons Forum and Aerospace Exposition (p. 1012). https://doi.org/10.2514/6.2013-1012

Enloe, C. L., McLaughlin, T. E., VanDyken, R. D., Kachner, K. D., Jumper, E. J., & Corke, T. C. (2003, January). *Mechanisms and responses of a single dielectric barrier plasma actuator*. 41st AIAA Aerospace Sciences Meeting and Exhibit (pp. 2003-1021). https://doi.org/10.2514/6.2003-1021

Erfani, R., Erfani, T., Utyuzhnikov, S. V., & Kontis, K. (2013). Optimisation of multiple encapsulated electrode plasma actuator. *Aerospace Science and Technology*, *26*(1), 120-127. https://doi.org/10.1016/j.ast.2012.02.020

Erfani, R., Zare-Behtash, H., Hale, C., & Kontis, K. (2015). Development of DBD plasma actuators: The double encapsulated electrode. *Acta Astronautica*, *109*, 132-143. https://doi.org/10.1016/j.actaastro.2014.12.016

Grundmann, S., & Tropea, C. (2007). Experimental transition delay using glow-discharge plasma actuators. *Experiments in Fluids*, *42*, 653-657. https://doi.org/10.1007/s00348-007-0256-8

Guo, Y., Li, Z., Chen, K., & Geng, X. (2023). Experimental investigation of the dynamic characteristics of the flow generated by a sliding dielectric barrier discharge in the flat plate boundary layer flow. *Physics of Fluids*, *35*(1). https://doi.org/10.1063/5.0134835

Hehner, M. T., Coutinho, G., Pereira, R. B. S., Benard, N., & Kriegseis, J. (2023). On the interplay of body-force distributions and flow speed for dielectric-barrier discharge plasma actuators. *Journal of Physics D: Applied Physics*, *56*(37), 375205. https://doi.org/10.1088/1361-6463/acdade

Huang, X., & Zhang, X. (2008). Streamwise and spanwise plasma actuators for flow-induced cavity noise control. *Physics of Fluids*, *20*(3). https://doi.org/10.1063/1.2890448

Jukes, T. N., & Choi, K. S. (2009). Control of unsteady flow separation over a circular cylinder using dielectric-barrier-discharge surface plasma. *Physics of Fluids*, *21*(9). https://doi.org/10.1063/1.3237151

Kazanskyi, P. N., Klimov, A. I., & Moralev, I. A. (2012). High-frequency actuator control of air flow near a circular cylinder: Impact of the discharge parameters on the cylinder aerodynamic drag. *High Temperature*, *50*(3), 323-330. https://doi.org/10.1134/S0018151X12030145

Kopiev, V. F., Akishev, Y. S., Belyaev, I. V., Berezhetskaya, N. K., Bityurin, V. A., Faranosov, G. A., Grushin, M. E., Klimov, A. I., Kopiev, V. A., Kossyi, I. A., Moralev, I. A., Ostrikov, N. N., Taktakishvili, M. I., Trushkin, N. I., & Zaytsev, M. Y. (2014). Instability wave control in turbulent jet by plasma actuators. *Journal of Physics D: Applied Physics*, 47(50), 505201. https://doi.org/10.1088/0022-3727/47/50/505201

Kozlov, A. V., & Thomas, F. O. (2011). Bluff-body flow control via two types of dielectric barrier discharge plasma actuation. *AIAA Journal*, *49*(9), 1919-1931. https://doi.org/10.2514/1.J050793

Lee, K., Kozato, Y., Kikuchi, S., & Imao, S. (2022).

Numerical simulation of flow control around a rectangular cylinder by dielectric barrier discharge plasma actuators. *Physics of Fluids*, *34*(7). https://doi.org/10.1063/5.0096067

Li, Y., Zhang, X., & Huang, X. (2010). The use of plasma actuators for bluff body broadband noise control. E*xperiments in Fluids*, *49*, 367-377. https://doi.org/10.1007/s00348-009-0806-3

Lombardi, A. J., Bowles, P. O., & Corke, T. C. (2013). Closed-loop dynamic stall control using a plasma actuator. *AIAA Journal*, *51*(5), 1130-1141. https://doi.org/10.2514/1.J051988

Luo, X., & Li, Y. (2022). Sliding discharge plasma jet actuators for circular-cylinder wake modification. *Modern Physics Letters B*, *36*(25), 2250130. https://doi.org/10.1142/S0217984922501305

Moayedi, H., Amanifard, N., & Deylami, H. M. (2023). Parametric study of DBD plasma actuator for heat transfer enhancement in flow over a flat plate at low Reynolds numbers. *Journal of Electrostatics*, *124*, 103825. https://doi.org/10.1016/j.elstat.2023.103825

Moreau, E. (2007). Airflow control by non-thermal plasma actuators. *Journal of Fhysics D: Applied Physics*, *40*(3), 605. https://doi.org/10.1088/0022-3727/40/3/S01

Nesaeian, M., & Homaeinezhad, M. R. (2023). Analytical input-output modelling of surface dielectric barrier discharge plasma actuator. *Journal of Physics D: Applied Physics*, *56*(46), 465204. https://doi.org/10.1088/1361-6463/acefe0

Niu, X., Chen, H., Li, Y., Jia, X., Zhang, Y., Yong, X., & Li, C. (2022). Design and performance of a small-scale acoustic wind tunnel at Wenzhou University for aerodynamic noise studies. *Applied Acoustics*, *199*, 109010. https://doi.org/10.1016/j.apacoust.2022.109010

Ogawa, T., Asada, K., Sato, M., Tatsukawa, T., & Fujii, K. (2022). Computational study of the plasma actuator flow control for an airfoil at pre-stall angles of attack. *Applied Sciences*, *12*(18), 9073. https://doi.org/10.3390/app12189073

Raffel, M., Willert, C. E., Scarano, F., Kähler, C. J., Wereley, S. T., & Kompenhans, J. (2018). *Particle image velocimetry: a practical guide*. Springer.

Rizzetta, D. P., & Visbal, M. R. (2010). Large-eddy simulation of plasma-based turbulent boundary-layer separation control. *AIAA Journal*, *48*(12), 2793-2810. https://doi.org/10.2514/1.J050014

Roth, J. R. (1995). Investigation of a uniform glow discharge plasma in atmospheric air. *NASA STI/Recon Technical Report N*, *96*, 11311.

Roth, J. R., Sherman, D. M., & Wilkinson, S. P. (2000). Electrohydrodynamic flow control with a glow-discharge surface plasma. *AIAA Journal*, *38*(7), 1166-1172. https://doi.org/10.2514/2.1110

Seth, U. K., Traoré, P., Duran-Olivencia, F. J., Moreau, E., & Vazquez, P. A. (2018). Parametric study of a DBD plasma actuation based on the Suzen-Huang model. *Journal of Electrostatics*, *93*, 1-9. https://doi.org/10.1016/j.elstat.2018.02.003

Sun, Q., Geng, X., Li, Z., Shi, Z., Sun, Z., & Cheng, K. (2023). Characteristics of a nanosecond pulsed sliding discharge plasma actuator at low pressure. *AIP Advances*, 13(7). https://doi.org/10.1063/5.0160843

Thomas, F. O., Corke, T. C., Iqbal, M., Kozlov, A., & Schatzman, D. (2009). Optimization of dielectric barrier discharge plasma actuators for active aerodynamic flow control. *AIAA Journal*, *47*(9), 2169-2178. https://doi.org/10.2514/1.41588

Thomas, F. O., Kozlov, A., & Corke, T. C. (2008). Plasma actuators for cylinder flow control and noise reduction. *AIAA Journal*, *46*(8), 1921-1931. https://doi.org/10.2514/1.27821

Uemura, T., Komuro, A., & Ono, R. (2023). Flow control around a pitching oscillation circular cylinder using a dielectric barrier discharge plasma actuator. *Journal of Physics D: Applied Physics*, *56*(12), 125202. https://doi.org/10.1088/1361-6463/acb720

Visbal, M. R. (2010). Strategies for control of transitional and turbulent flows using plasma-based actuators. *International Journal of Computational Fluid Dynamics*, *24*(7), 237-258. https://doi.org/10.1080/10618562.2010.533123

Wang, J. J., Choi, K. S., Feng, L. H., Jukes, T. N., & Whalley, R. D. (2013). Recent developments in DBD plasma flow control. *Progress in Aerospace Sciences*, *62*, 52-78. https://doi.org/10.1016/j.paerosci.2013.05.003

Wang, Y. S., Wu, B., Gao, C., Yuan, X. S., Zhang, Y. X., Wang, N., Xu, Z. Y., Li, Y. Q., Wang, Y. L., & Hao, D. D. (2022). Lagrangian analysis of the flow induced by a dielectric barrier discharge plasma actuator array under burst mode actuation. *AIP Advances*, *12*(11). https://doi.org/10.1063/5.0124082

Wojewodka, M. M., White, C., & Kontis, K. (2020). Effect of permittivity and frequency on induced velocity in ac-DBD surface and channel plasma actuators. *Sensors and Actuators A: Physical*, *303*, 111831. https://doi.org/10.1016/j.sna.2020.111831

Yan, X., Zhang, Y., & Li, Y. (2024). Noise control of blunt flat-plate using slit and dielectric barrier discharge Plasma. *AIAA Journal*, 1-15. https://doi.org/10.2514/1.J063259

Yu, H., Cui, X., Li, G., & Zheng, J. (2023). Numerical investigation of flow separation control over rotor blades using plasma actuator. *AIAA Journal*, *61*(3), 1151-1167. https://doi.org/10.2514/1.J062428

Yu, J., Liu, H., Xu, D., & Chen, F. (2014). Investigation of the DBD plasma effect on flat plate flow. *Plasma Science and Technology*, *16*(3), 197. https://doi.org/10.1088/1009-0630/16/3/05

Zhang, X., Cui, Y. D., Qu, F., & Li, H. X. (2022). Acoustic streaming in water induced by an asymmetric dielectric-barrier-discharge plasma actuator at the initiation stage. *Physics of Fluids*, *34*(1). https://doi.org/10.1063/5.0076231